Chinese Journal of Physics 78 (2022) 435–452

Contents lists available at ScienceDirect

Chinese Journal of Physics

journal homepage: www.sciencedirect.com/journal/chinese-journal-of-physics

Boundary layer flow of micropolar nanofluid towards a permeable stretching sheet in the presence of porous medium with thermal radiation and viscous dissipation

Muhammad Salman Kausar [a], Abid Hussanan [b,*], Muhammad Waqas [c], Mustafa Mamat [a]

[a] Faculty of Informatics and Computing, University Sultan Zainal Abidin (Kampus Gong Badak), Kuala Terengganu, Terengganu 21300, Malaysia
[b] Department of Mathematics, Division of Science and Technology, University of Education, Lahore, 54000, Pakistan
[c] NUTECH School of Applied Science and Humanities, National University of Technology, Islamabad 44000, Pakistan

ARTICLE INFO

Keywords:
Nanofluid
Thermal radiation
Suction/injection
Porous dissipation

ABSTRACT

Nanofluids are a novel new generation of fluids to improve the heat transfer capabilities of conventional heat transfer fluids. The thermo–physical properties of these fluids are very classic in comparison to common fluids. However, one of the most crucial drawbacks for classical nanofluid models is that they cannot describe a class of fluids that have certain microscopic characteristics arising from the micro–rotation and local structure of the fluid elements. In the present study, a numerical investigation has been carried out to discuss the laminar two–dimensional heat transfer flow of micropolar nanofluid through a porous medium over a stretching sheet with viscous dissipation and thermal radiation containing copper (Cu) nanoparticles and water is considered as a base fluid. The mathematical model has been formulated based on Tiwari–Das nanofluid model. The basic equations are transmitted into a set of nonlinear ordinary differential equations using similarity transformation, and then the numerical solution is evaluated by using the Runge–Kutta fourth–order procedure. The relevant results of velocity, angular velocity and temperature are shown visually and discussed quantitatively in detail. The micro–rotation parameter enhances the velocity and temperature of the fluid. The boundary parameter declines the velocity but shows the reverse effects for angular velocity. The suction parameter decreases the velocity, but the reverse impacts are seen for the injection parameter. The graphical outcomes also show that the momentum boundary layer thickness increases with the values of volume fraction and porosity. The temperature is growing due to enhancing the Eckert number and radiation parameter.

1. Introduction

Generally, nanofluids are divided into two phases, one is a solid phase, which contains nanomaterials, and the other phase is known as a liquid phase, which consists of the base fluid. Nanofluids are more advance as compared to the base fluid because they contain unique properties and exclusive parameters. Nanofluids possess many outstanding properties which have higher thermal conductivity,

* Corresponding author.
E-mail address: abid.hussanan@ue.edu.pk (A. Hussanan).

https://doi.org/10.1016/j.cjph.2022.06.027
Received 7 August 2021; Received in revised form 21 May 2022; Accepted 29 June 2022
Available online 1 July 2022
0577-9073/

Nomenclature

$(C_p)_f$	Base fluid specific heat capacity $[J\cdot kg^{-1}\cdot K^{-1}]$
$(C_p)_s$	Nanoparticles specific heat capacity $[J\cdot kg^{-1}\cdot K^{-1}]$
$(C_p)_{nf}$	Nanofluid specific heat capacity $[J\cdot kg^{-1}\cdot K^{-1}]$
Ec	Eckert number
F'	Dimensionless velocity
j	Micro–inertia density $[m^2]$
K_f	Base fluid thermal conductivity $[W\cdot m^{-1}\cdot K^{-1}]$
K_s	Nanoparticles thermal conductivity $[W\cdot m^{-1}\cdot K^{-1}]$
K_{nf}	Nanofluid thermal conductivity $[W\cdot m^{-1}\cdot K^{-1}]$
K^*	Permeability of the porous medium $[m^2]$
k^*	Mean absorption coefficient
M	Micro–rotation parameter
M_R	Vortex viscosity $[kg\cdot m^{-1}\cdot s^{-1}]$
N	Angular velocity $[s^{-1}]$
Nr	Radiation parameter
Nu_x	Nusselt number
n	Boundary parameter
Pr	Prandtl number
Pm	Porosity parameter
q_r	Radiative heat flux $[W\cdot m^{-2}]$
S	Suction/injection parameter
T	Temperature of the fluid $[K]$
T_∞	Ambient temperature $[K]$
T_0	Positive constant $[K\cdot m^{-2}]$
u	$x-$ component of velocity
v	$y-$ component of velocity

Greek symbols

ρ_f	Base fluid density $[kg\cdot m^{-3}]$
ρ_s	Nanoparticles density $[kg\cdot m^{-3}]$
ρ_{nf}	Nanofluid density $[kg\cdot m^{-3}]$
μ_f	Base fluid dynamic viscosity $[kg\cdot m^{-1}\cdot s^{-1}]$
μ_{nf}	Nanofluid dynamic viscosity $[kg\cdot m^{-1}\cdot s^{-1}]$
γ_{nf}	Spin-gradient viscosity $[kg\cdot m\cdot s^{-1}]$
φ	Nanoparticle volume fraction
ξ	Similarity variable
σ^*	Stefan-Boltzmann constant
θ	Dimensionless temperature
ψ	Stream function
$\in$	Ratio of constants

Subscripts

f	Base fluid
nf	Nanofluid
s	Solid particle nanofluid
w	Condition at wall
∞	Condition at infinity

viscosity and heat transmission. Many metallic and non–metallic nanofluid models are investigated due to their higher thermal performance. Recently, nanofluids technology attracted many scientists toward it due to its unique industrial applications like a chemical process, cooling process, power looms, and heat generation. Choi [1] was the pioneer one to introduce nanofluids. Later on, Eastman et al. [2] worked on the nanofluid thermal conductivity and heat transfer. Shafiq et al. [3] examined the bioconvective tangent hyperbolic magnetohydrodynamics (MHD) nanofluid flow with Newtonian heating. Tlili et al. [4] employed several slips results on MHD non–Newtonian nanofluid over a spherical shape cylinder enclosed in a porous media under chemical radiation effects. Haider et al. [5] theoretically and numerically investigated that the nanoparticle shape impacts on water–based aluminum oxide nanofluid toward a solid cylinder with heat–transmission effects. Khamliche et al. [6] reported the laser development of high thermal conductivity through *Cu* nanoparticles on nanofluids. Kotha et al. [7] scrutinized the impact of thermal radiation on engine oil nanofluid flow moving over a permeable wedge under convective heating with the help of Keller–Box technique. Gangadhar et al. [8] applied the spectral relaxation method to investigate the two-dimensional boundary layer flow of a nanofluid over a stretching plane. They pointed out that the temperature and nanoparticles volume fraction profiles decline with liquids of greater Prandtl numbers and the local Nusselt number upsurges with the growth in the heat absorption parameter. Recently, Kotha et al. [9] and Gangadhar et al. [10] claimed the nanofluid flow which is containing the gyrotactic microbes on the boundary layer surface. The Lorentz force and convective heating of radiative second–grade nanofluid moving over a Riga plate was introduced by the Gangadhar et al. [11]. The characteristics of nanofluids are extensively investigated in the literature [12–23].

Micropolar fluids have an inner structure or composed of a family of non–symmetric stress tensor fluids that can be regarded as polar fluids. Eringen [24] proposed that micropolar fluid theory considers the locally organized microscopic effect and the micro––rotating effect of liquid particles and a statistic model for non–Newtonian fluid behaviors. Research suggests that fluid action can easily be defined in a wide variety of applications, such as blood flow, colloidal suspension solutions, shear flows, liquid crystals, turbulent shear flows and porous media etc. Yusuf et al. [25] elucidated the steady micropolar fluid film due to entropy generation embedded in porous substrate with slip constraints. Muthtamilselvan et al. [26] conveyed the micropolar fluid under natural convection flow of heat source. The boundary layer flow of micropolar nanofluid with wall temperature due to natural convection is pointed out by Swalmeh et al. [27] by using the Keller–Box method. Moreover, Bhat and Katagi [28] developed a porous and non––porous disk the flow of two–dimensional micropolar fluid. Ahmad et al. [29] discussed a comprehensive study on micropolar fluid with the porous medium over a rotating cone. Nanofluid of mixed bio–convection bound to a micropolar fluid is numerically compiled by Zadeh et al. [30]. Recently, several researchers have studied the various physical parameters of micropolar nanofluids [31–44].

Boundary layer flows are used in various manufacturing applications, including liquid films, cables, plastic films, cables, crystal making, the cooling process of metals, uninterrupted filament extrusion from tint, the winding roll, liquefied dynamics, and many other applications of industrial zone. The rate of cooling firmly convinces the outcome with particular properties of elegance. Mass transport is also used in various structures and processes that facilitate the molecular and heat flux transfer of atoms and molecules. It is also specified that chemicals should be delivered and separated from natural and artificial sources through decontamination of the chemical pandemic. The linear stretching surface boundary layer flow is also considered [45–49], with many others cited. The various measurements of fluid flow and heat transfer are investigated in these experiments. In addition to the boundary layer flow encouraged by the expanded board, it encloses the electronic chips, extrusion phase, paper processing, ceramic, glass–fiber, and many others. Wide–scale, consistent movement under adverse pressure gradient in turbulent borders before flow separation. Eich and Kahler [50] gave the principle of consistent motions with a pressure gradient in turbulent boundary layers. Guo et al. [51] confirmed the convergent and divergent riblets in a laminar boundary layer flow due to secondary flow. The stretching flow problem was considered absolute in various ways, such as the heat transfer, mass transfer, MHD impacts inflows with or without suction/injection parameters on the sheet. The reference list of such fluids is pervasive, and some efforts in this area can be listed in the studies [52–55]. These studies have analyzed the role of heat transfer and viscous dissipation and have shown that both dynamics substantially influence thermal transfer by stimulating it.

Viscous dissipation is an essential factor in the flow of energy and regulated the temperature profile of the heat transfer procedure. The reliability of the viscous dissipation effect is determined by whether the plate is frozen or heated. Some common examples of energy transfer analysis arise in the developments of electronic devices, metals fluid, heating and cooling processes of metals and metalloids, nuclear reactors, and power generation. The concept of viscous dissipation by applying the perturbation method in natural convection is granted to Gebhart [56]. He pointed out that natural convection flow is incomplete without the influence of viscous dissipation for greater values of gravitational forces and Prandtl number fluids. Later on, Roja et al. [57] stated that the entropy generation can be improved with the aspects of viscous dissipation, magnetism and radiative heat flux through an inclined channel. Hussanan et al. [58] obtained the analytical solution for suction and injection flow of a viscoplastic fluid in the presence of viscous dissipation. Neeraja et al. [59] analyzed the MHD Casson liquid flow with convective boundary conditions and viscous dissipation due to a deformable channel. Hamid et al. [60] examined the particulate suspensions transport phenomena in the magnetite ferrofluid past a permeable non–isothermal moving surface with the viscous dissipation effect. Ajibade and Umar [61] conducted the boundary layer thickness and viscous dissipation on Couette flow through thermal conductivity and flexible viscosity.

A literature survey indicates that abundant studies are available discussing the micropolar flow over a stretching sheet. However, the studies about micropolar nanofluid flow over a stretching sheet with viscous dissipation through a porous medium are limited. This research is intended to scrutinize the steady laminar two-dimensional micropolar nanofluids boundary layer flow in the existence of a porous medium that has thermal and viscous dissipation to a stretching sheet with suction/injection impacts. The basic equations are transmitted into a set of nonlinear ordinary differential equations using similarity transformation, and then numerical solution is evaluated using the Runge–Kutta fourth–order procedure. By the graphical illustrations, permanent parameters influenced on the fluid flow are explained. Present analysis covers the characteristically important mechanical and engineering roles of porous medium such as mining, rock materials, cooling reactors etc. The constantly porous surface of fluid film caused the movement that is produced in mathematical model.

2. Problem formulation

Consider a steady two-dimensional micropolar nanofluid flow over a stretching sheet. The coordinate system is assumed to define the $x-$ axis along the sheet and $y-$ axis is the coordinate normal to the sheet. The stretching velocity $u_w(x)$ and the ambient fluid velocity $u_e(x)$ are assumed to vary linearly from the stagnation point, i.e., $u_w(x) = cx$ and $u_e(x) = ax$, where a and c are constants with $c > 0$. It is also expected that the temperature of the stretching sheet is $T_s(x) = T_\infty + T_0 x^2$ [49], where T_0 is positive constant. The boundary layer equations for micropolar nanofluid followed by [12, 44] can be described as

$$\frac{\partial u}{\partial x} + \frac{\partial v}{\partial y} = 0, \tag{1}$$

$$u\frac{\partial u}{\partial x} + v\frac{\partial u}{\partial y} = u_e\frac{du_e}{dx} + \left(\nu_{nf} + \frac{M_R}{\rho_{nf}}\right)\frac{\partial^2 u}{\partial y^2} + \frac{M_R}{\rho_{nf}}\frac{\partial N}{\partial y} - \frac{\nu_{nf}}{K^*}(u - u_e), \tag{2}$$

$$u\frac{\partial N}{\partial x} + v\frac{\partial N}{\partial y} = \frac{\gamma_{nf}}{\rho_{nf} j}\frac{\partial^2 N}{\partial y^2} - \frac{M_R}{\rho_{nf} j}\left(2N + \frac{\partial u}{\partial y}\right), \tag{3}$$

$$u\frac{\partial T}{\partial x} + v\frac{\partial T}{\partial y} = \frac{K_{nf}}{(\rho C_p)_{nf}}\frac{\partial^2 T}{\partial y^2} - \frac{1}{(\rho C_p)_{nf}}\frac{\partial q_r}{\partial y} + \frac{\mu_{nf} + M_R}{(\rho C_p)_{nf}}\left[\frac{u^2}{K^*} + \left(\frac{\partial u}{\partial y}\right)^2\right]. \tag{4}$$

For the above physical phenomenon, the following associate boundary conditions are considered as

$$\begin{aligned} u = \;& u_w(x) = cx, \;\; v = V_0, \;\; N = -n\frac{\partial u}{\partial y}, \; T = T_s(x) = T_\infty + T_0 x^2 \text{ at } y = 0, \\ u \to \;& u_e(x) = ax, \; N \to 0, \;\; T \to T_\infty \text{ as } y \to \infty, \end{aligned} \tag{5}$$

where u and v representing the velocity components in the $x-$ and $y-$ directions, respectively, V_0 surface mass transfer velocity. Furthermore, ρ_{nf}, μ_{nf}, ν_{nf}, $(\rho C_p)_{nf}$, K_{nf} and γ_{nf} are the effective density, dynamic viscosity, kinematic viscosity, specific heat capacity, thermal conductivity and spin–gradient viscosity of the nanofluid, respectively, and are defined [27,44] as follows

$$\begin{aligned} &\rho_{nf} = (1-\varphi)\rho_f + \rho_s\varphi, \;\; \mu_{nf} = \frac{\mu_f}{(1-\varphi)^{2.5}}, \;\; \nu_{nf} = \frac{\mu_{nf}}{\rho_{nf}}, \\ &(\rho C_p)_{nf} = (1-\varphi)(\rho C_p)_f + \varphi(\rho C_p)_s, \\ &\frac{K_{nf}}{K_f} = \frac{K_s + 2K_f - 2\varphi(K_f - K_s)}{K_s + 2K_f + \varphi(K_f - K_s)}, \;\; \gamma_{nf} = \left(\mu_{nf} + \frac{M_R}{2}\right)j. \end{aligned} \tag{6}$$

All other symbols and quantities are given in the nomenclature. Thermophysical properties of base fluids and nanoparticles [32,62] are given in Table 1. Here $M_R = 0$ resembles the position of viscous fluid. The boundary parameter n differs in the range $0 \le n \le 1$. The case $n = 0$ relates density of the particle is sufficiently large so that the microelements close to the sheet are incapable to rotate. The case $n = 1/2$ indicates weak concentration of microelement and $n = 1$ is used for the modeling of turbulent flows. Following Magyari and Pantokratoras [63], we adopt the Rosseland approximation for radiative flux

$$q_r = -\frac{4\sigma^*}{3k^*}\frac{\partial T^4}{\partial y}, \tag{7}$$

where σ^* is the Stefan–Boltzmann constant and k^* is known as the mean absorption coefficient. Expanding T^4 in a Taylor series about T_∞ as

$$T^4 \cong T_\infty^4 + 4T_\infty^3(T - T_\infty) + 6T_\infty^2(T - T_\infty)^2 + \ldots.,$$

and then ignoring higher–order expressions, we get

$$T^4 \cong 4T_\infty^3 T - 3T_\infty^4. \tag{8}$$

Now differentiating Eq. (7) on both sides, we obtain

$$\frac{\partial q_r}{\partial y} = -\frac{16\sigma^* T_\infty^3}{3k^*}\frac{\partial^2 T}{\partial y^2}. \tag{9}$$

By engaging Eq. (9) into Eq. (4), we get

$$u\frac{\partial T}{\partial x} + v\frac{\partial T}{\partial y} = \frac{1}{(\rho C_p)_{nf}}\left[\left(\frac{16\sigma^* T_\infty^3}{3k^*} + K_{nf}\right)\frac{\partial^2 T}{\partial y^2}\right] + \frac{\mu_{nf} + M_R}{(\rho C_p)_{nf}}\left[\frac{u^2}{K^*} + \left(\frac{\partial u}{\partial y}\right)^2\right]. \tag{10}$$

By Implementation of a stream function ψ as

$$u = \frac{\partial \psi}{\partial y}, \;\; v = -\frac{\partial \psi}{\partial x}. \tag{11}$$

By using transformation

$$\xi = \left(\frac{c}{\nu_f}\right)^{\frac{1}{2}} y,\ u = cxF'(\xi),\ v = -(c\nu_f)^{\frac{1}{2}} F(\xi),\ N = cx\left(\frac{c}{\nu_f}\right)^{\frac{1}{2}} G(\xi), \theta = \frac{T - T_\infty}{T_s - T_\infty}, \tag{12}$$

we obtained the following ordinary differential equations

$$\frac{\rho_f}{\rho_{nf}}\left(\frac{\mu_{nf}}{\mu_f} + M\right) F''' + FF'' - (F')^2 + \frac{\rho_f M}{\rho_{nf}} G' + \in^2 - \frac{\mu_{nf}}{\mu_f}\frac{\rho_f Pm}{\rho_{nf}}(F' - \in) = 0, \tag{13}$$

$$\frac{\rho_f}{\rho_{nf}}\left(\frac{\mu_{nf}}{\mu_f} + \frac{M}{2}\right) G'' + FG' - F'G - \frac{\rho_f}{\rho_{nf}}(2MG - MF'') = 0, \tag{14}$$

$$\frac{(\rho C_p)_f}{\Pr(\rho C_p)_{nf}}\left(Nr + \frac{K_{nf}}{K_f}\right)\theta'' + F\theta' - 2F'\theta + \frac{(\rho C_p)_f\left(\frac{\mu_{nf}}{\mu_f} + M\right)}{(\rho C_p)_{nf}} Ec\left(PmF'^2 + F''^2\right) = 0. \tag{15}$$

By using Eq. (12), the associated boundary conditions become

$$\begin{aligned} F(0) = &\ S,\ F'(0) = 1,\ G(0) = -nF''(0),\ \theta(0) = 1, \\ F'(\infty) = &\ \in = \frac{a}{c},\ G(\infty) = \theta(\infty) = 0, \end{aligned} \tag{16}$$

where prime signifies the derivative to ξ, M is the micro–rotation parameter, Pr is the Prandtl number, $\in$ is the ratio of constants a and c, Nr is the radiation parameter, Pm is the porosity parameter, Ec is the Eckert number, S is the mass flux constant with suction (positive values) and for injection (negative values) and prescribed as follows

$$M = \frac{M_R}{\mu_f}, Pr = \frac{\mu_f C_p}{K_f}, Nr = \frac{16\sigma^* T_\infty^3}{3K_f k^*}, Ec = \frac{c^2}{T_0 (C_p)_f}, Pm = \frac{\nu_f}{K^* c}, S = \frac{V_0}{\sqrt{c\nu_f}}, j = \frac{\nu_f}{c}.$$

The definition of skin friction coefficient C_{fx}, the couple stress C_n and the Nusselt number (heat flux) Nu_x is outlined as

$$C_{fx} = \frac{\tau_w}{\rho_{nf} u_w^2},\ C_n = \frac{x}{c}\left(\frac{\partial N}{\partial y}\right)_{y=0},\ Nu_x = \frac{x\, q_w}{K_{nf}(T_s - T_\infty)}. \tag{17}$$

In the above notations, the wall shear stress τ_w and the heat flux q_w are mentioned as

$$\tau_w = \left[(\mu_{nf} + M_R)\frac{\partial u}{\partial y} + M_R N\right]_{y=0},\quad q_w = -\left[K_{nf}\frac{\partial T}{\partial y} + q_r\right]_{y=0}. \tag{18}$$

By utilizing Eq. (12) similarity variables, the skin friction, couple stress and Nusselt number (heat flux) in the dimensionless system are expressed as

$$\mathrm{Re}_x^{1/2} C_{fx} = \left(\frac{\rho_f}{\rho_{nf}}\right)\left[\frac{\mu_{nf}}{\mu_f} + (1-n)M\right] F''(0), \mathrm{Re}_x^{-1} C_n = G'(0), Nu_x \mathrm{Re}_x^{-1/2} = -\frac{K_f}{K_{nf}}\left(\frac{K_{nf}}{K_f} + Nr\right)\theta'(0). \tag{19}$$

where $\mathrm{Re}_x = \frac{u_w x}{\nu_f}$ denotes the Reynolds number.

3. Graphical outcomes

A numerical approach has been made to consider the impact of micropolar water–based nanofluid over a stretching sheet through adjustable suction ($S > 0$) or injection ($S < 0$) in the existence of thermal radiation and viscous dissipation with a porous medium. The velocity $F'(\xi)$, angular velocity $G(\xi)$, and temperature $\theta(\xi)$ fields are demonstrated by numerous monitoring parameters, such as parameter of constant ratio ($\in$), suction/injection parameter (S), boundary parameter (n), nanoparticle volume fraction (φ), porosity parameter (Pm), Eckert number (Ec), micro–rotation parameter (M) and radiation parameter (Nr). The numerical outcomes are

Table 1
Thermophysical properties of base fluids and nanoparticles [32,62]

Physical properties	Water	Kerosene oil	Copper(Cu)
$\rho[kg \cdot m^{-3}]$	997.1	783	8933
$C_p[J \cdot kg^{-1} \cdot K^{-1}]$	4179	2090	385
$K[W \cdot m^{-1} \cdot K^{-1}]$	0.613	0.15	401
Pr	6.2	21	–

computed and presented alongside graphical representations. Figs. 1–6 are explaining the impression of various parameters on velocity $F^{'}(\xi)$, Figs. 7–9 exhibited the angular velocity $G(\xi)$ with different parameters effect, and the consequence of diverse parameters on the temperature field $\theta(\xi)$ are seen in Figs. 10–14. Moreover, the Prandtl number ($\Pr = 6.2$) is fixed in each case. In order to validate the precision of our present data, studies have reported an association with the existing findings of Gangadhar et al. [12], Fauzi et al. [43] and Hussanan et al. [44] as seen in Table 2–4. A comparison of skin friction$\left(\mathrm{Re}_x^{\frac{1}{2}}C_{fx}\right)$ for viscous fluid and porous sheet in the imaginariness of suction/injection is arranged in Table 2. Table 3 demonstrates the comparative impacts of the skin friction coefficient for Cu water–based micropolar nanofluid on embedded stretching sheet. Table 4 determines the comparative impressions of couple stress ($\mathrm{Re}_x^{-1}C_n$) for nanofluid under study. The results obtained in the present work are well established to show close consistency with the previously published results.

Fig. 1 displays the linear velocity $F^{'}(\xi)$ profile with variation in constant ratio parameter ($\in$). The constant ratio parameter is considering a ratio of two constant a and c such that $\left(\in = \frac{a}{c}\right)$. The velocity profile is represented for distinctive values of $\in$ when $S = n = Ec = Nr = 0.5, M = Pm = 1.0, \Pr = 6.2, \ \varphi = 0.002$ are considered constant. From this figure, it is evident that, in case of progressive values of constant ratio parameter $\in > 1$, the velocity of micropolar nanofluid increases, and the boundary layer thickness also increases with the rising of $\in$, while in case of $\in < 1$ the fluid velocity deteriorizing with the decline $\in$ in the boundary layer. Moreover, the graph shows a straight horizontal line at $\in = 1$. Fig. 2 displays the velocity $F^{'}(\xi)$ profile for distinction values of micro–rotation parameter (M) for fixed values of $S = n = Ec = Nr = 0.5$, $\Pr = 6.2$, $\varphi = 0.002, \in = 0.2$, $Pm = 1.0$. We can see that the velocity $F^{'}(\xi)$ profile increases when the micro–rotation parameter (M) is enhanced. This phenomenon is that the momentum boundary layer is increased when we raise the micro–rotation parameter (M) that expresses the fluids motion and, therefore, the velocity $F^{'}(\xi)$ profile is boosted. In Fig. 3, the effects of boundary parameter (n) on velocity $F^{'}(\xi)$ profile is portrayed when$S = Ec = Nr = 0.5, \in = 0.2, Pm = M = 1.0, \Pr = 6.2, \ \varphi = 0.002$ are fixed. It has seen that the velocity $F^{'}(\xi)$ decline with a growth in the boundary parameter. When we raise the boundary parameter (n), conflict in the fluid motion is familiarized. Fig. 4 illustrates the velocity $F^{'}(\xi)$ field rises for as we increase the amount of nanoparticle volume fraction (φ) for fixed $n = S = Ec = Nr = 0.5$, $Pm = M = 1.0$. Physically, the volume fraction (φ) increased with rising the boundary layer thickness for micropolar nanofluid on the stretching sheet. Fig. 5 portrays the velocity $F^{'}(\xi)$ for porosity parameter (Pm), when the other parameters $n = S = Ec = Nr = 0.5, \in = 0.2$, $\Pr = 6.2, \Pr = 6.2$, $\varphi = 0.002, \in = 0.2, M = 1.0$ are fixed. The velocity $F^{'}(\xi)$ shows declining behavior when the values of porosity parameter (Pm) are increased. The reason is that the porosity is creating a drag force that is engaged reverse the track of the flow. Fig. 6 describes the impression of suction/injection parameter (S) on velocity $F^{'}(\xi)$ profile when the other parameters $Nr = Ec = 0.5$, $n = 0.2, M = Pm = 1.0, \varphi = 0.002$, $\Pr = 6.2$, $\in = 0.2$ are taken constant. The consequences display that the velocity $F^{'}(\xi)$ field sharp falls with the rise of the suction parameter ($S > 0$) on the sheet for different suction parameter values of the suction parameter, and the boundary layer thickness also declines due to the rising suction parameter. On the contrary, the linear velocity $F^{'}(\xi)$ has a definite flow structure for the injection parameter ($S < 0$), and the boundary layer thickness is enhancing with falling ($S < 0$) parameter values at particular values of injection parameter. It is exciting to indicate that during injection, the buoyancy disparate flows lead the assisting flows for all the micropolar nanofluid values on the stretching sheet.

The volume fraction parameter effects (φ) are significant on the micro–rotation velocity $G(\xi)$ in the boundary layer regime, as displayed in Fig. 7 when $S = Ec = Nr = 0.5, \in = n = 0.2$, $Pm = 1.0, M = 0.1$, $\Pr = 6.2$ are assumed as constant for enhancing values (φ) on the stretching sheet. The microrotation distribution neighboring to the sheet surface declines, after that rises in some recess and then rises throughout the sheet area's flow field. We conclude that (φ) is to spin of microelements in the micropolar nanofluid. Fig. 8 displays the impact of the boundary parameter (n) on the angular velocity $G(\xi)$. It is verified that the angular velocity $G(\xi)$ enhances with the rising values of (n) while the other parameters are kept constant$\in = 0.2$, $Pm = 1.0 S = Ec = Nr = 0.5, M = 0.1$, $\Pr = 6.2, \varphi =$

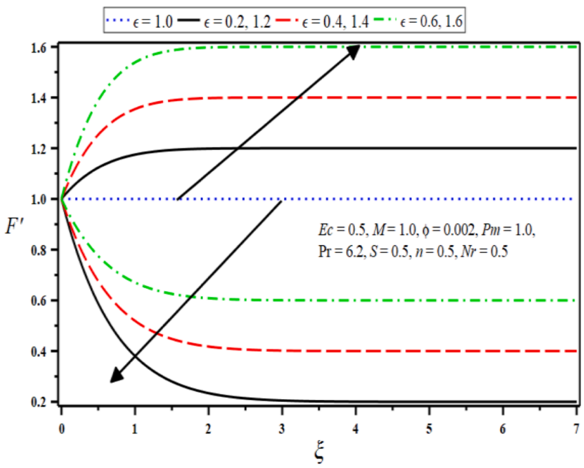

Fig. 1. Effects of $\in$ on $F^{'}$.

Table 2

Evaluation of $Re_x^{\frac{1}{2}}C_{fx}$ for K and n when $\phi = 0$, and $S = 0$.

$n = 0$				$n = 0.5$			
M	Fauzi et al. [43]	Gangadhar et al. [12]	Present study	Fauzi et al. [43]	Gangadhar et al. [12]	Hussanan et al. [44]	Present study
0	−1.0000	−1.0000	−1.0000	−1.0000	−1.0000	−1.0000	−1.0000
1	−1.3680	−1.3680	−1.3680	−1.2248	−1.2248	−1.2248	−1.2248
2	−1.6225	−1.6216	−1.6216	−1.4159	−1.4145	−1.4142	−1.4145
4	−2.0075	−2.0054	−2.0054	−1.7381	−1.7333	−1.7321	−1.7333

Table 3

Evaluation of $Re_x^{\frac{1}{2}}C_{fx}$ for S when $M = 2$, $n = 0.5$, $Pr = Pm \in = Ec = x = 0$ for Cu.

$\varphi = 0.05$				$\varphi = 0.1$			$\varphi = 0.2$		
S	Fauzi et al. [43]	Gangadhar et al. [12]	Present study	Fauzi et al. [43]	Gangadhar et al. [12]	Present study	Fauzi et al. [43]	Gangadhar et al. [12]	Present study
0	−1.6258	−1.6178	−1.6177	−1.7726	−1.7668	−1.7668	−1.9466	−1.9427	−1.9427
1	−2.4026	−2.3992	−2.3992	−2.7136	−2.7118	−2.7118	−3.1041	−3.1032	−3.1032
2	−3.3896	−3.3890	−3.3890	−3.9183	−3.9181	−3.9181	−4.5954	−4.5954	−4.5954
2.5	−3.9362	−3.9360	−3.9360	−4.5830	−4.58\9	−4.5829	−5.4147	−5.4146	−5.4146
3	−4.5061	−4.5061	−4.5061	−5.2741	−5.2741	−5.2741	−6.2637	−6.2637	−6.2637

Table 4

Evaluation of $Re_x^{-1}C_n$ for S when $M = 2$, $n = 0.5$, $Pr = Pm = \in = Ec = x = 0$ for Cu.

$\varphi = 0.05$				$\varphi = 0.1$			$\varphi = 0.2$		
S	Fauzi et al. [43]	Gangadhar et al. [12]	Present study	Fauzi et al. [43]	Gangadhar et al. [12]	Present study	Fauzi et al. [43]	Gangadhar et al. [12]	Present study
0	−0.3273	−0.3271	−0.3271	−0.3903	−0.3908	−0.3902	−0.4719	−0.4718	−0.4718
1	−0.7201	−0.7195	−0.7195	−0.9196	−0.9192	−0.9192	−1.2040	−1.2038	−1.2038
2	−1.4359	−1.4357	−1.4357	−1.9191	−1.9190	−1.9190	−2.6397	−2.6397	−2.6397
2.5	−1.9366	−1.9365	−1.9365	−2.6255	−2.6254	−2.6254	−3.6648	−3.6648	−3.6648
3	−2.5381	−2.5381	−2.5381	−3.4770	−3.4770	−3.4770	−4.9042	−4.9042	−4.9042

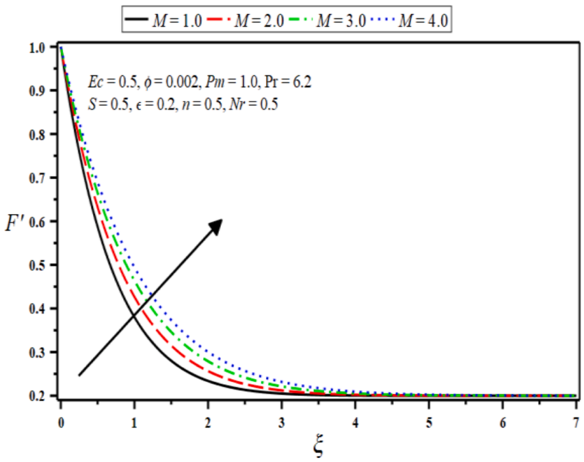

Fig. 2. Effects of M on F'.

0.02. We can claim that a different bent plane with a high boundary parameter (n) has created a thicker boundary layer across the sheet. In Fig. 9, the angular velocity $G(\xi)$ graph is drawn against micro–rotation parameters (M) when$S = Ec = Nr = 0.5$,$n = 0.1$, $Pr = 6.2$, $\varphi = 0.02$,$\in= 0.2$, $Pm = 1.0$ are fixed. A remarkable change occurs because the microrotation distribution closes the surface, first shrinkages after that surges in some recess and then growths all over the flow field of angular velocity $G(\xi)$ when micro–rotation parameter (M) increases for micropolar nanofluid.

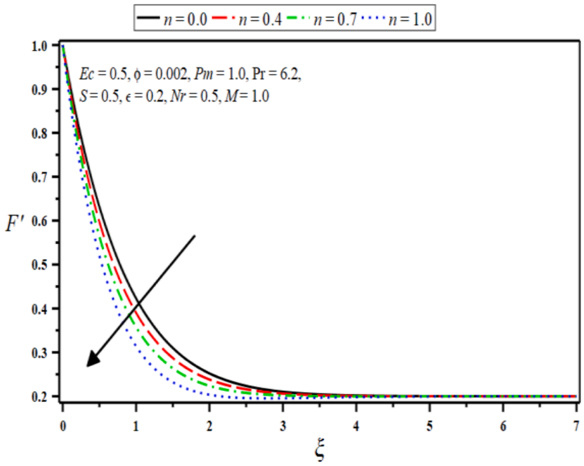

Fig. 3. Effects of n on F'.

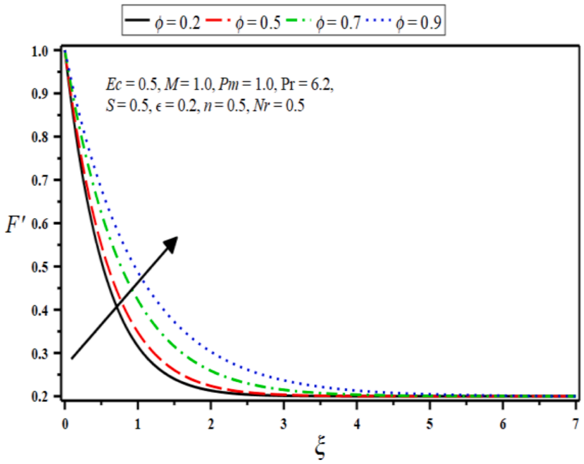

Fig. 4. Effects of φ on F'.

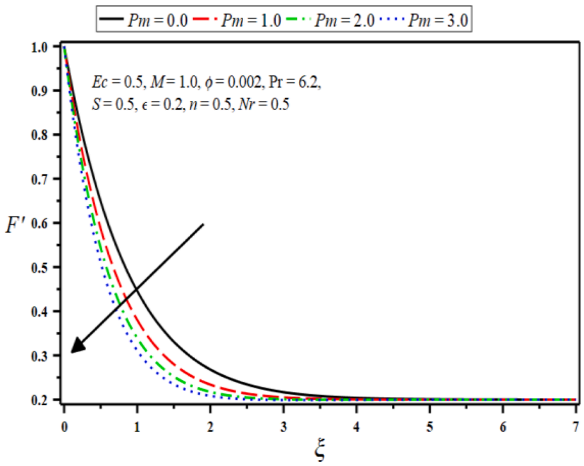

Fig. 5. Effects of Pm on F'.

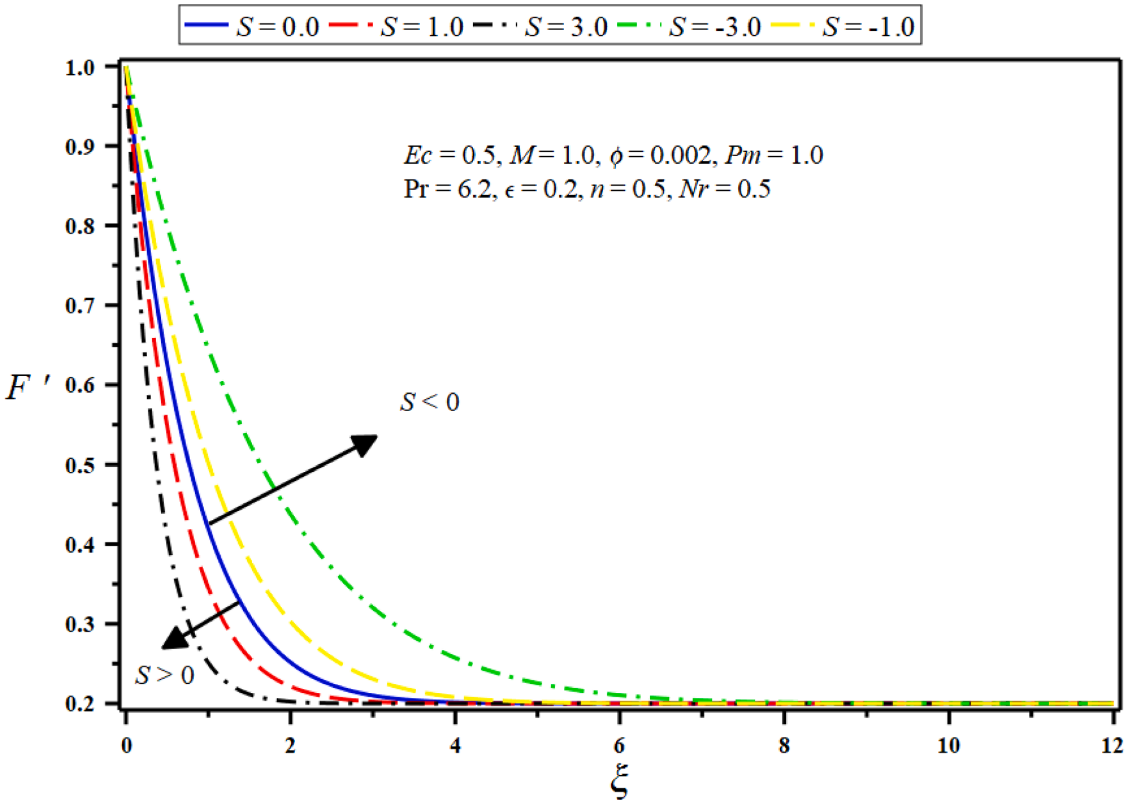

Fig. 6. Effects of S on F'.

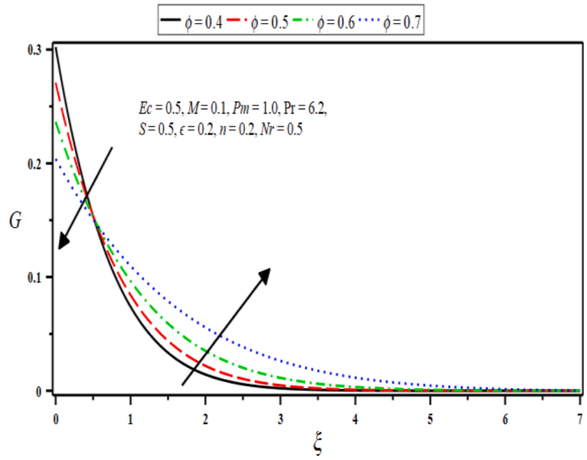

Fig. 7. Effects of φ on G.

The outcomes of the volume fraction parameter (φ) on temperature field is shown in Fig. 10. While the parameters $S = n = Pm = 0.5, M = 1.0, Ec = 0.01$, $\Pr = 6.2, \in = 0.2$, $Nr = 5.0$ are fixed for increasing (φ). It is prominent that the thermal boundary layer width drops when φ is amplified for the stretching canal. The variation of the micropolar nanofluid temperature field for diverse porosity parameter values is shown in Fig. 11. In the growth of the porosity parameter (Pm) some variables are kept constant like that $n = S = 0.5, M = 0.1, Ec = 0.01, \varphi = 0.02, \Pr = 6.2, Nr = 5.0, \in = 0.2$. It is witnessed that the temperature spreads when Pm is enlarged for the micropolar nanofluid stretching channel. The porosity parameter drives the fluid particles from the upper to the dropping temperature, so intensifying temperature. The implications of the Eckert number (Ec) on a temperature field are seen in Fig. 12. The other regulatory parameters are established as $Nr = 5.0, \in = 0.2, M = 1.0, \varphi = 0.002, Pm = n = S = 0.5, \Pr = 6.2$. When the Eckert number (Ec) for viscous fluid increases, the thermal boundary layer's thickness significantly rises for the stretching surface. The Eckert parameter (Ec)

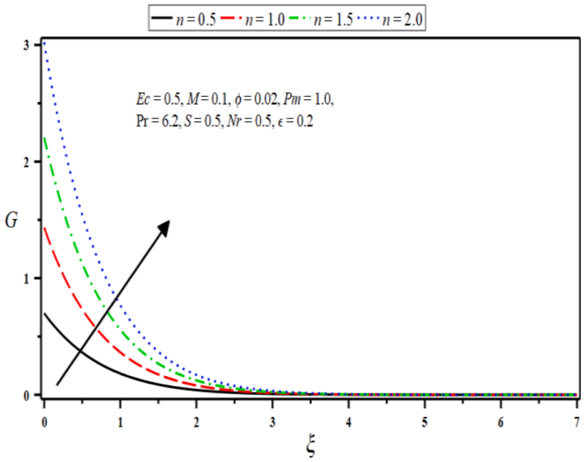

Fig. 8. Effects of $n$on G.

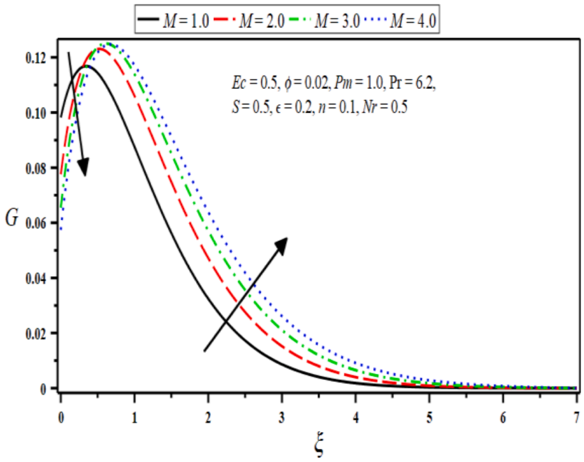

Fig. 9. Effects of M on G.

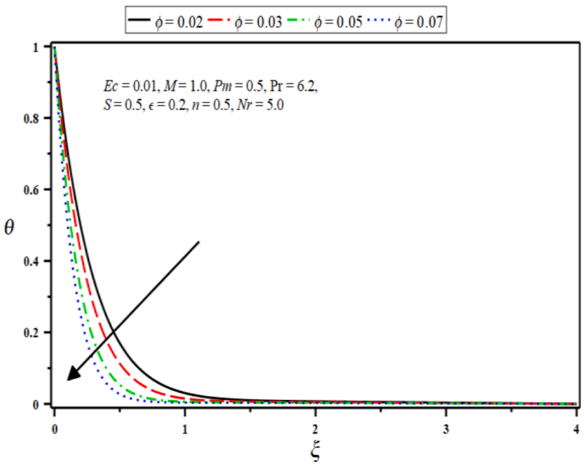

Fig. 10. Effects of φ on θ.

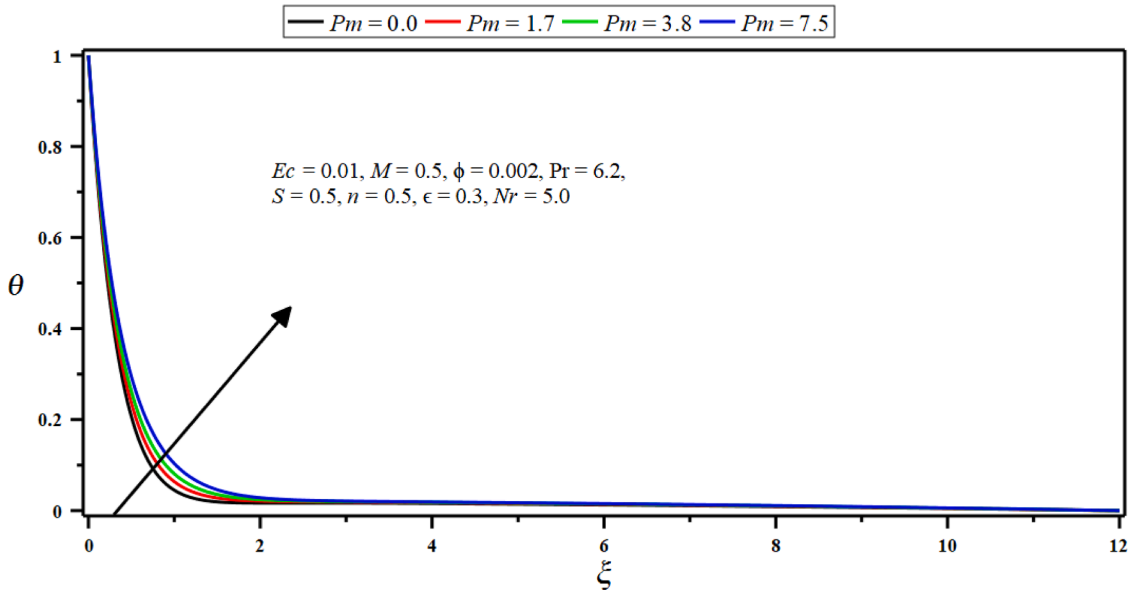

Fig. 11. Effects of Pm on θ.

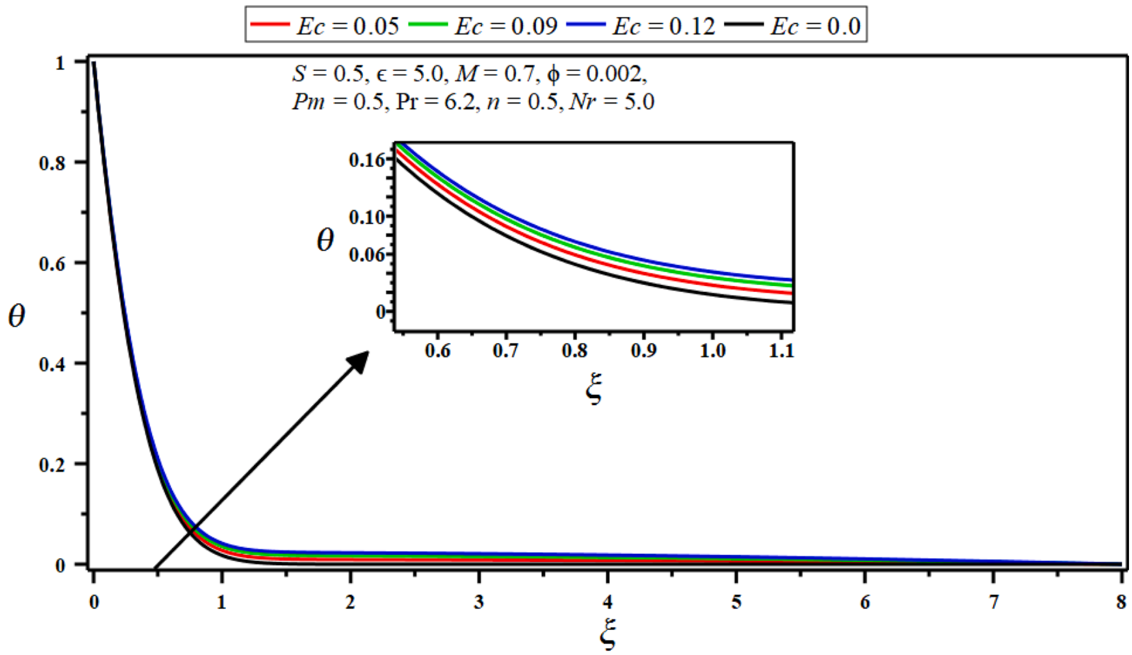

Fig. 12. Effects of Ec on θ.

for viscous fluid effect tends to grow the fluid temperature and considerably buildups the sheet's thermal boundary layer width. The outcomes of micro–rotation parameter (M) on the temperature distribution are exemplified in Fig. 13. The impacts of micro–rotation parameter (M) are defined by the presumptuous values of other parameters as $Ec = 0.05$, $\varphi = 0.002$, $Pm = n = S = 0.5$, $\Pr = 6.2$, $Nr = 5.0$, $\in = 0.2$. It is noticed that for micropolar nanofluid, as micro–rotation parameter upsurges, the thermal boundary layer breadth intensifications for embedded stretching sheet. The influence of radiation parameter (Nr) on fluid temperature field is offered in Fig. 14. The discussion takes place for the continuous values of the other parameters, for example $n = Pm = S = 0.5$ $\Pr = 6.2$, $\in = 0.2$, $\varphi = 0.002$. As a result, the temperature area raises the radiation parameter for the embedded layer considerably.

The skin friction coefficient under constant ratio parameter ($\in$) is sketched in Fig. 15. We recognized that the skin friction coefficient has increased tendency for ascent values of constant ratio parameter ($\in$). It is also observed from Fig. 16 that with the increase in micro–rotation parameters (M), the magnitude of skin friction coefficient increases. Furthermore, skin friction coefficient in case of $\in$

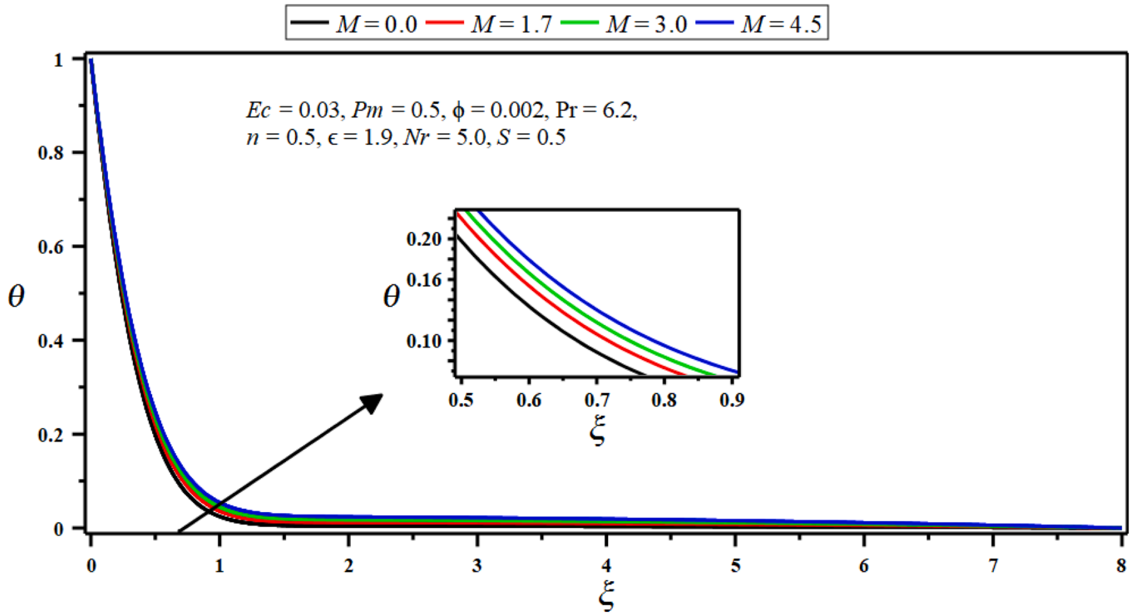

Fig. 13. Effects of M on θ.

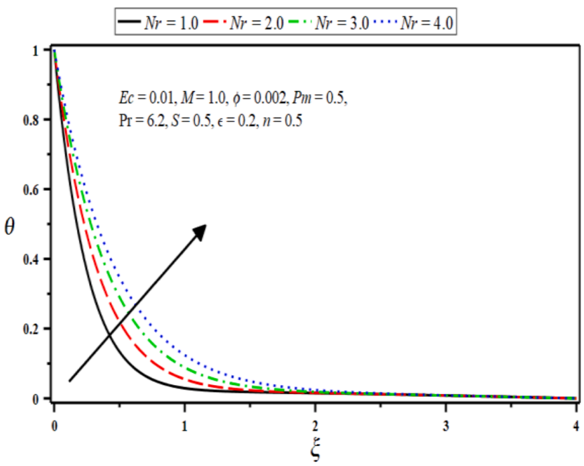

Fig. 14. Effects of Nr on θ.

> 1 increases more rapidly than that in case of $\in< 1$. Skin friction coefficient in case of $\in> 1$ increases with increasing values of porosity parameter (Pm), but decreases in case of $\in< 1$ as shown in Fig. 17. On the other hand, Fig. 18 is plotted to analyze the consequence of micro–rotation parameters (M) over couple stress. It is indicated that in case of $\in> 1$, the couple stress decreases as the micro–rotation parameter (M) increases, but the couple stress increases as the micro–rotation parameter (M) increases, when $\in< 1$. Fig. 19 examines the behavior of boundary parameter (n) on couple stress. It is founded that couple stress reduces via larger values of boundary parameter (n) in case of $\in< 1$. In addition, it is clear from this that, for $n = 0$, couple stress shows similar behavior for both cases $\in> 1$ and $\in< 1$. Physically, $n = 0$ relates density of the particle is sufficiently large so that the microelements close to the sheet are incapable to rotate. The consequence of porosity parameter (Pm) on couple stress is illustrated by Fig. 20. This figure indicates that the impact of the porosity parameter (Pm) creates resistance in case of $\in< 1$ which reduces the couple stress. Moreover, the couple stress presents opposite behavior against the porosity parameter (Pm) in case of $\in> 1$.

Fig. 21 is the plotted for Nusselt number for different values of Eckert number (Ec) in both cases of $\in> 1$ and $\in< 1$. It is founded that Nusselt number decreases with increasing Eckert number (Ec) in both cases of $\in> 1$ and $\in< 1$. Moreover, Fig. 22 is plotted to analyze the consequence of radiation parameter (Nr) on Nusselt number. It is indicated that in both cases of $\in> 1$ and $\in< 1$, the Nusselt number increases as the radiation parameter (Nr). Physically, higher values of radiation parameter (Nr) lead to the convection mode dominates over the conduction mode in the system. The effects of the volume fraction parameter (φ) and porosity parameter (Pm) on Nusselt number for both cases of constant ratio parameter such as $\in> 1$ and $\in< 1$ are presented in Figs. 23 and 24, respectively. The Nusselt

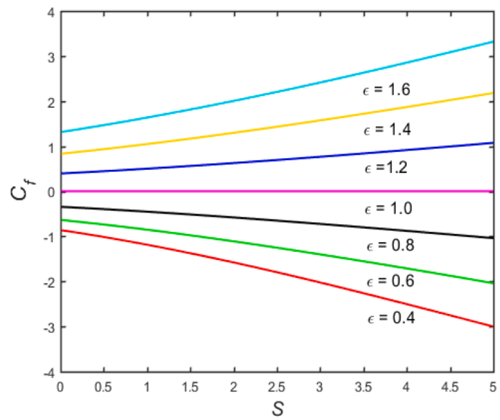

Fig. 15. Effects of $\in$ on C_f.

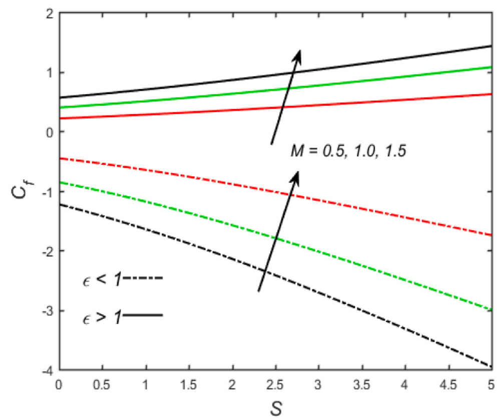

Fig. 16. Effects of M on C_f.

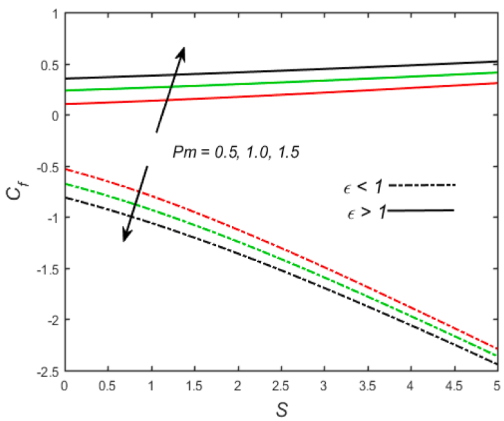

Fig. 17. Effects of Pm on C_f.

number decreases with the increase in the value of volume fraction parameter (φ), and is maximum for the smallest values of volume fraction parameter (φ). Moreover, the Nusselt number behaves similarly for porosity parameter (Pm) as for volume fraction parameter (φ) in both case of constant ratio parameter ($\in > 1$ and $\in < 1$).

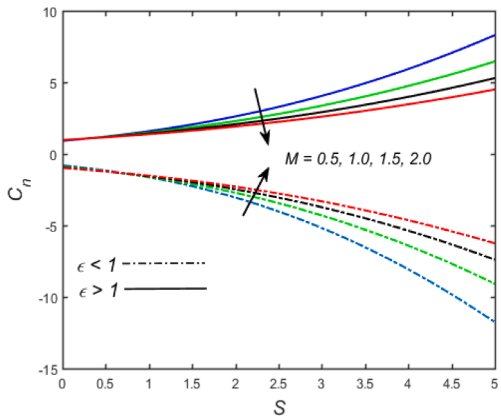

Fig. 18. Effects of M on C_n.

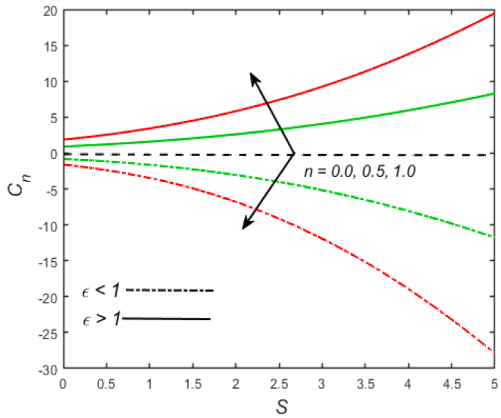

Fig. 19. Effects of n on C_n.

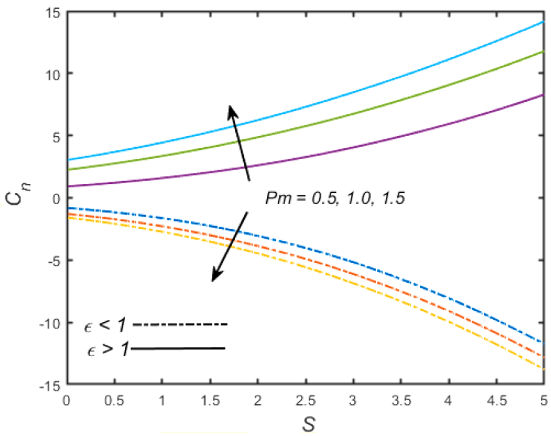

Fig. 20. Effects of Pm on C_n.

4. Final remarks

Numerical investigation has been carried out to discuss the laminar two–dimensional heat transfer flow of micropolar nanofluid through a porous medium with viscous dissipation and thermal radiation containing copper (Cu) over a stretching sheet The suitable similarity transformation is employed to transform the governing equations into ordinary differential equations. The transformed ordinary differential equations are numerically solved by Runge–Kutta fourth–order approach through Maple. The results obtained in

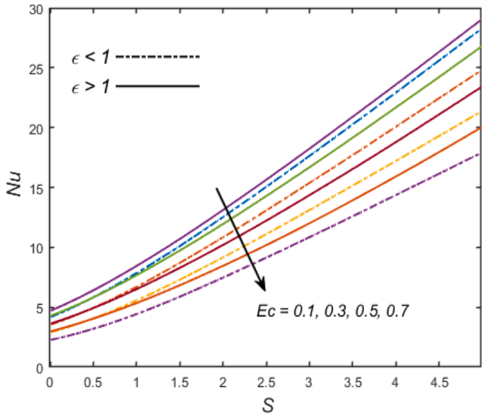

Fig. 21. Effects of *Ec* on *Nu*.

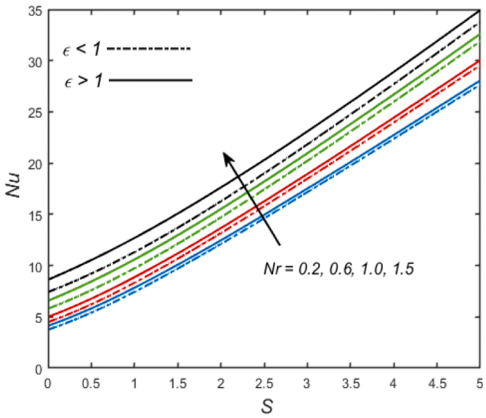

Fig. 22. Effects of *Nr* on *Nu*.

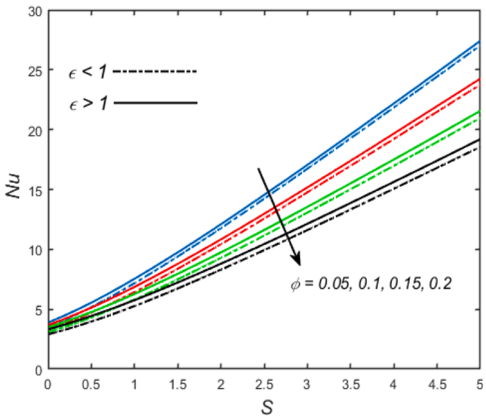

Fig. 23. Effects of φ on *Nu*.

this investigation are of great interest in different areas of science and technology where the surface layers are being stretched. Some of the exciting results of the present study are

i Linear velocity increases for $\in > 1$, $S < 0$ and decreases for $\in < 1$, $S > 0$ on the stretching sheet.
ii Momentum layer enhances with M, φ and declines for n, Pm on the stretching sheet.
iii Angular velocity shows the approximate increasing behavior for φ, n and Mparameters.

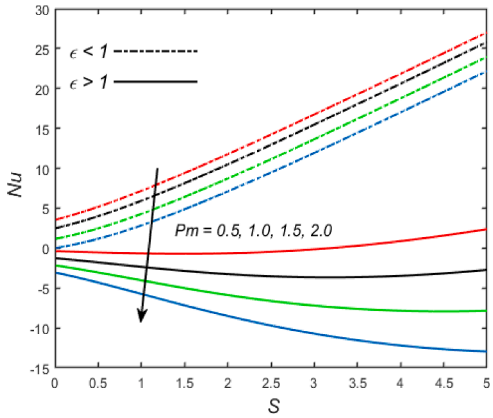

Fig. 24. Effects of Pm on Nu.

iv Thermal boundary layer width is growing for Pm,Ec,$M$and decreases for φ.
v The numerical values of $\mathrm{Re}_x^{\frac{1}{2}}C_{fx}$ and $\mathrm{Re}_x^{-1}C_n$ decline for the growing values of $M$and S.
vi Nusselt number decreases with the increase in the values of volume fraction parameter.

Declaration of Competing Interest

The authors declare that they have no known competing financial interests or personal relationships that could have appeared to influence the work reported in this paper.

References

[1] S.U. Choi, Enhancing Thermal Conductivity of Fluids With Nanoparticles (No. ANL/MSD/CP-84938; CONF-951135-29), Argonne National Lab., IL (United States), 1995.
[2] J.A. Eastman, S.U.S. Choi, S. Li, W. Yu, L.J. Thompson, Anomalously increased effective thermal conductivities of ethylene glycol-based nanofluids containing copper nanoparticles, Appl. Phys. Lett. 78 (6) (2001) 718–720, https://doi.org/10.1016/j.ijmecsci.2017.07.048.
[3] A. Shafiq, Z. Hammouch, T.N. Sindhu, Bioconvective MHD flow of tangent hyperbolic nanofluid with Newtonian heating, Int. J. Mech. Sci. 133 (2017) 759–766.
[4] I. Tlili, W.A. Khan, I. Khan, Multiple slips effects on MHD SA-Al2O3 and SA-Cu non-Newtonian nanofluids flow over a stretching cylinder in porous medium with radiation and chemical reaction, Results Phys. 8 (2018) 213–222, https://doi.org/10.1016/j.rinp.2017.12.013.
[5] S. Haider, A.S. Butt, I.S. Muhammad, A. Ali, Y.Z. Li, S.M.A. Naqvi, M.A. Qaiser, Impact of nano-particles shapes on Al2O3-water nanofluid flow due to a stretching cylinder, Int. J. Numer. Methods Heat Fluid Flow 30 (5) (2019) 2809–2832, https://doi.org/10.1108/HFF-02-2019-0113.
[6] T. Khamliche, S. Khamlich, M.K. Moodley, B.M. Mothudi, M. Henini, M. Maaza, Laser fabrication of Cu nanoparticles based nanofluid with enhanced thermal conductivity: experimental and molecular dynamics studies, J. Mol. Liq. 323 (1) (2020), 114975, https://doi.org/10.1016/j.molliq.2020.114975.
[7] G. Kotha, K. Kukkamalla, S.M. Ibrahim, Effect of thermal radiation on engine oil nanofluid flow over a permeable wedge under convective heating: Keller box method, Multidiscip. Model. Mater. Struct (2019), https://doi.org/10.1108/MMMS-03-2018-0047.
[8] K. Gangadhar, T. Kannan, G. Sakthivel, K. DasaradhaRamaiah, Unsteady free convective boundary layer flow of a nanofluid past a stretching surface using a spectral relaxation method, Int. J. Ambient Energy 41 (6) (2020) 609–616.
[9] G. Kotha, V.R. Kolipaula, M.V.S. Rao, S. Penki, A.J. Chamkha, Internal heat generation on bioconvection of an MHD nanofluid flow due to gyrotactic microorganisms, Eur. Phys. J. Plus 135 (7) (2020) 1–19, https://doi.org/10.1140/epjp/s13360-020-00606-2.
[10] K. Gangadhar, K.B. Lakshmi, T. Kannan, A.J. Chamkha, Stefan blowing on chemically reactive nano-fluid flow containing gyrotactic microorganisms with leading edge accretion (or) ablation and thermal radiation, Indian J. Phys. (2021) 1–14, https://doi.org/10.1007/s12648-021-02179-x.
[11] K. Gangadhar, M.A. Kumari, A.J. Chamkha, EMHD flow of radiative second-grade nanofluid over a riga plate due to convective heating: revised Buongiorno's nanofluid model, Arab. J. Sci. Eng. (2021) 1–11, https://doi.org/10.1007/s13369-021-06092-7.
[12] K. Gangadhar, T. Kannan, P. Jayalakshmi, Magnetohydrodynamic micropolar nanofluid past a permeable stretching/shrinking sheet with Newtonian heating, J. Braz. Soc. Mech. Sci. Eng. 39 (11) (2017) 4379–4391.
[13] M.V.S. Rao, K. Gangadhar, A.J. Chamkha, P. Surekha, Bioconvection in a convectional nanofluid flow containing gyrotactic microorganisms over an isothermal vertical cone embedded in a porous surface with chemical reactive species, Arab. J. Sci. Eng. 46 (3) (2021) 2493–2503.
[14] K. Gangadhar, R.E. Nayak, M.V.S. Rao, T. Kannan, Nodal/Saddle stagnation point slip flow of an aqueous convectional magnesium oxide–gold hybrid nanofluid with viscous dissipation, Arab. J. Sci. Eng. 46 (3) (2021) 2701–2710.
[15] K. Gangadhar, B.K. Lakshmi, T. Kannan, A.J. Chamkha, Entropy generation in magnetized bioconvective nanofluid flow along a vertical cylinder with gyrotactic microorganisms, J. Nanofluids 9 (4) (2020) 302–312.
[16] K. Gangadhar, K.B. Lakshmi, T. Kannan, Thermal transport of magnetized Cu−Fe3O4/water hybrid nanofluid over a curved surface, Int. J. Appl. Comput. Math. 7 (5) (2021) 1–21.
[17] B.C. Prasannakumara, Assessment of the local thermal non-equilibrium condition for nanofluid flow through porous media: a comparative analysis, Indian J. Phys. (2021) 1–9.
[18] R.P. Gowda, A. Rauf, R.N. Kumar, B.C. Prasannakumara, S.A. Shehzad, Slip flow of Casson–Maxwell nanofluid confined through stretchable disks, Indian J. Phys. (2021) 1–9.
[19] B.C. Prasannakumara, Numerical simulation of heat transport in Maxwell nanofluid flow over stretching sheet considering magnetic dipole effect, Partial Differ. Equ. Appl. Math. (2021), 100064.
[20] R.P. Gowda, R.N. Kumar, B.C. Prasannakumara, B. Nagaraja, B.J. Gireesha, Exploring magnetic dipole contribution on ferromagnetic nanofluid flow over a stretching sheet: an application of Stefan blowing, J. Mol. Liq. 335 (2021), 116215.
[21] R.P. Gowda, H.B. Mallikarjuna, B.C. Prasannakumara, R.N. Kumar, P.T. Manjunatha, Dynamics of thermal Marangoni stagnation point flow in dusty Casson nanofluid, Int. J. Model. Simul. (2021) 1–9.

[22] Y.Q. Song, A. Hamid, M.I. Khan, R.P. Gowda, R.N. Kumar, B.C. Prasannakumara, M.Y. Malik, Solar energy aspects of gyrotactic mixed bioconvection flow of nanofluid past a vertical thin moving needle influenced by variable Prandtl number, Chaos, Solit. Fract. 151 (2021), 111244.
[23] S.M. Aminossadati, B. Ghasemi, Natural convection cooling of a localised heat source at the bottom of a nanofluid-filled enclosure, Eur. J. Mech.-B/Fluids 28 (5) (2009) 630–640.
[24] A.C. Eringen, Theory of micropolar fluids, J. Math. Mech. (1966) 1–18.
[25] T.A. Yusuf, R.N. Kumar, B.C. Prasannakumara, S.O. Adesanya, Irreversibility analysis in micropolar fluid film along an incline porous substrate with slip effects, Int. Commun. Heat Mass Transf. 126 (2021), 105357.
[26] M. Muthtamilselvan, K. Periyadurai, D.H. Doh, Effect of uniform and nonuniform heat source on natural convection flow of micropolar fluid, Int. J. Heat Mass Transf. 115 (2017) 19–34, https://doi.org/10.1016/j.ijheatmasstransfer.2017.06.134.
[27] M.Z. Swalmeh, H.T. Alkasasbeh, A. Hussanan, M. Mamat, Heat transfer flow of Cu-water and Al2O3-water micropolar nanofluids about a solid sphere in the presence of natural convection using Keller-box method, Results Phys. 9 (2018) 717–724, https://doi.org/10.1016/j.rinp.2018.03.033.
[28] A. Bhat, N.N. Katagi, Micropolar fluid flow between a non-porous disk and a porous disk with slip: Keller-box solution, Ain Shams Eng. J. 11 (1) (2020) 149–159.
[29] S. Ahmad, K. Ali, H. Bashir, Interaction of micropolar fluid structure with the porous media in the flow due to a rotating cone, Alex. Eng. J. 60 (1) (2020) 1249–1257, https://doi.org/10.1016/j.aej.2020.10.048.
[30] S.M.H. Zadeh, S.A.M. Mehryan, M.A. Sheremet, M. Izadi, M. Ghodrat, Numerical study of mixed bio-convection associated with a micropolar fluid, Therm. Sci. Eng. Progress (2020), 100539, https://doi.org/10.1016/j.tsep.2020.100539.
[31] A. Roja, B.J. Gireesha, B.C. Prasannakumara, MHD micropolar nanofluid flow through an inclined channel with entropy generation subjected to radiative heat flux, viscous dissipation and multiple slip effects, Multidiscip. Model. Mater. Struct. 16 (6) (2020) 1475–1496, https://doi.org/10.1108/MMMS-12-2019-0235.
[32] M. Alizadeh, A.S. Dogonchi, D.D. Ganji, Micropolar nanofluid flow and heat transfer between penetrable walls in the presence of thermal radiation and magnetic field, Case Stud. Thermal Eng. 12 (2018) 319–332, https://doi.org/10.1016/j.csite.2018.05.002.
[33] S.S. Ghadikolaei, K. Hosseinzadeh, D.D. Ganji, Numerical study on magnetohydrodynic CNTs-water nanofluids as a micropolar dusty fluid influenced by nonlinear thermal radiation and joule heating effect, Powder Technol. 340 (2018) 389–399, https://doi.org/10.1016/j.powtec.2018.09.023.
[34] H. Hashemi, Z. Namazian, S.M.H. Zadeh, S.A.M. Mehryan, MHD natural convection of a micropolar nanofluid flowing inside a radiative porous medium under LTNE condition with an elliptical heat source, J. Mol. Liq. 271 (2018) 914–925, https://doi.org/10.1016/j.molliq.2018.09.010.
[35] M. Izadi, S.A.M. Mehryan, M.A. Sheremet, Natural convection of CuO-water micropolar nanofluids inside a porous enclosure using local thermal non-equilibrium condition, J. Taiwan Inst. Chem. Eng. 88 (2018) 89–103, https://doi.org/10.1016/j.jtice.2018.04.019.
[36] Z. Shah, S. Islam, T. Gul, E. Bonyah, M.A. Khan, The electrical MHD and hall current impact on micropolar nanofluid flow between rotating parallel plates, Results Phys. 9 (2018) 1201–1214, https://doi.org/10.1016/j.rinp.2018.01.064.
[37] E.O. Fatunmbi, H.A. Ogunseye, P. Sibanda, Magnetohydrodynamic micropolar fluid flow in a porous medium with multiple slip conditions, Int. Commun. Heat Mass Transf. 115 (2020), 104577, https://doi.org/10.1016/j.icheatmasstransfer.2020.104577.
[38] N. Abbas, S. Nadeem, M.Y. Malik, Theoretical study of micropolar hybrid nanofluid over Riga channel with slip conditions, Phys. A: Stat. Mech. Appl. 551 (2020), 124083, https://doi.org/10.1016/j.physa.2019.124083.
[39] L.A. Lund, Z. Omar, I. Khan, Mathematical analysis of magnetohydrodynamic (MHD) flow of micropolar nanofluid under buoyancy effects past a vertical shrinking surface: dual solutions, Heliyon 5 (9) (2019) e02432.
[40] S. Nadeem, M.N. Khan, N. Muhammad, S. Ahmad, Mathematical analysis of bio-convective micropolar nanofluid, J. Comput. Des. Eng. 6 (3) (2019) 233–242.
[41] A. Hussanan, M.Z. Salleh, I. Khan, S. Shafie, Convection heat transfer in micropolar nanofluids with oxide nanoparticles in water, kerosene and engine oil, J. Mol. Liq. 229 (2017) 482–488.
[42] B. Ali, S. Hussain, Y. Nie, L. Ali, S.U. Hassan, Finite element simulation of bioconvection and cattaneo-Christov effects on micropolar based nanofluid flow over a vertically stretching sheet, Chinese J. Phys. 68 (2020) 654–670.
[43] E.L.A. Fauzi, S. Ahmad, I. Pop, Flow over a permeable stretching sheet in micropolar nanofluids with suction, AIP Conf. Proc. 1605 (1) (2014) 428–433.
[44] A. Hussanan, M.Z. Salleh, I. Khan, Microstructure and inertial characteristics of a magnetite ferrofluid over a stretching/shrinking sheet using effective thermal conductivity model, J. Mol. Liq. 255 (2018) 64–75.
[45] G. K. Ramaiah, D. Kotha, K Thangavelu, MHD rotating flow of a Maxwell fluid with Arrhenius activation energy and non-Fourier heat flux model Heat Transf. 49 (4) (2020) 2209–2227.
[46] G. Kotha, V.S.R. Munagala, V.K. Damerla, R.S.R. Gorla, Newtonian heating effect on laminar flow of Casson fluids: thermal analysis, Heat Transf. 49 (4) (2020) 2390–2405.
[47] M.V. Subba Rao, K. Gangadhar, P.R Sobhana Babu, Sutterby fluid flow past a stretching sheet embedded in a porous media with viscous dissipation, Int. J. Ambient Energy (2021), https://doi.org/10.1080/01430750.2021.1945491.
[48] K. Gangadhar, M. Venkata Subba Rao, K. Venkata Ramana, S. Kumar, A.J. Chamkha, Thermal slip flow of a three-dimensional Casson fluid embedded in a porous medium with internal heat generation, J. Nanofluids 10 (1) (2021) 58–66.
[49] M.I. Afridi, M. Qasim, S. Shafie, Entropy generation in hydromagnetic boundary flow under the effects of frictional and Joule heating: exact solutions, Eur. Phys. J. Plus 132 (9) (2017) 404.
[50] F. Eich, C.J. Kähler, Large-scale coherent motions in turbulent boundary layers under an adverse pressure gradient up to flow separation, Int. J. Heat Fluid Flow 85 (2020), 108645, https://doi.org/10.1016/j.ijheatfluidflow.2020.108645.
[51] T. Guo, S. Zhong, T. Craft, Secondary flow in a laminar boundary layer developing over convergent-divergent riblets, Int. J. Heat Fluid Flow 84 (2020), 108598, https://doi.org/10.1016/j.ijheatfluidflow.2020.108598.
[52] H. Zhang, Y. Wu, Y. Li, Mechanism of compressor airfoil boundary layer flow control using nanosecond plasma actuation, Int. J. Heat Fluid Flow 80 (2019), 108502, https://doi.org/10.1016/j.ijheatfluidflow.2019.108502.
[53] A. Pantokratoras, Four usual errors made in investigation of boundary layer flows, Powder Technol. 353 (2019) 505–508, https://doi.org/10.1016/j.powtec.2019.05.060.
[54] R.S. Saif, T. Muhammad, H. Sadia, R. Ellahi, Boundary layer flow due to a nonlinear stretching curved surface with convective boundary condition and homogeneous-heterogeneous reactions, Phys. A: Stat. Mech. Appl. 551 (2020), 123996, https://doi.org/10.1016/j.physa.2019.12399.
[55] K.V. Ramana, K. Gangadhar, T. Kannan, A.J. Chamkha, Cattaneo–Christov heat flux theory on transverse MHD Oldroyd-B liquid over nonlinear stretched flow, J. Therm. Anal. Calorim. (2021) 1–11, https://doi.org/10.1007/s10973-021-10568-x.
[56] B. Gebhart, Effects of viscous dissipation in natural convection, J. Fluid Mech. 14 (2) (1962) 225–232.
[57] A. Roja, B.J. Gireesha, B.C. Prasannakumara, MHD micropolar nanofluid flow through an inclined channel with entropy generation subjected to radiative heat flux, viscous dissipation and multiple slip effects, Multidiscip. Model. Mater. Struct. 16 (6) (2020) 1475–1496, https://doi.org/10.1108/MMMS-12-2019-0235.
[58] A. Hussanan, M.Z. Salleh, I. Khan, S. Shafie, Analytical solution for suction and injection flow of a viscoplastic Casson fluid past a stretching surface in the presence of viscous dissipation, Neural Comput. Appl. 29 (2018) 1507–1515.
[59] A. Neeraja, R.R. Devi, B. Devika, V.N. Radhika, M.K. Murthy, Effects of viscous dissipation and convective boundary conditions on magnetohydrodynamics flow of casson liquid over a deformable porous channel, Results Eng. 4 (2019), 100040, https://doi.org/10.1016/j.rineng.2019.100040.
[60] R.A. Hamid, R. Nazar, K. Naganthran, I. Pop, Dusty ferrofluid transport phenomena towards a non-isothermal moving surface with viscous dissipation, Chinese J. Phys. 75 (2022) 139–151, https://doi.org/10.1016/j.cjph.2021.11.002.

[61] A.O. Ajibade, A.M. Umar, Effects of viscous dissipation and boundary wall thickness on steady natural convection Couette flow with variable viscosity and thermal conductivity, Int. J. Thermofluids 7 (2020), 100052, https://doi.org/10.1016/j.ijft.2020.100052.
[62] U. Khan, N. Ahmed, S.T. Mohyud-Din, Numerical investigation for three-dimensional squeezing flow of nanofluid in a rotating channel with lower stretching wall suspended by carbon nanotubes, Appl. Therm. Eng. 113 (2017) 1107–1117.
[63] E. Magyari, A. Pantokratoras, Note on the effect of thermal radiation in the linearized Rosseland approximation on the heat transfer characteristics of various boundary layer flows, Int. Commun. Heat Mass Transf. 38 (2011) 554–556.